



# A highly sensitive ascorbic acid sensor using a Ni–Pt electrode

Yu-Ching Weng<sup>a,\*</sup>, Yuan-Gee Lee<sup>b</sup>, Yu-Lun Hsiao<sup>a</sup>, Chiu-Yue Lin<sup>c</sup>

<sup>a</sup> Department Chemical Engineering, Feng Chia University, Taichung 40724, Taiwan

<sup>b</sup> Department of Automation Engineering and Institute of Mechatronic Systems, Chien-Kuo Institute of Technology, Changhua 50094, Taiwan

<sup>c</sup> Department Environmental Engineering and Science, Feng Chia University, Taichung 40724, Taiwan

## ARTICLE INFO

### Article history:

Received 17 June 2011

Received in revised form 20 August 2011

Accepted 22 August 2011

Available online 30 August 2011

### Keywords:

Ni–Pt

Sensing mechanism

Erinaceous surface

Sensitivity

Reliability

## ABSTRACT

An amperometric sensor that measured ascorbic acid by the oxidation of the ascorbic acid on a Ni–Pt electrode was fabricated. The Ni component of the Ni–Pt alloy played a crucial role as a modifier that developed an erinaceous surface, which enlarged the sensing area and increased the sensitivity of the electrode. The Pt<sub>82</sub>Ni<sub>18</sub> electrode exhibited the best sensitivity of 333  $\mu\text{A cm}^{-2} \text{mM}^{-1}$  for ascorbic acid sensing. This electrode was further tested for reproducibility of the sensitivity, endurance, and interference; it exhibited excellent performance compared with electrodes reported in the literature.

© 2011 Elsevier Ltd. All rights reserved.

## 1. Introduction

Albert Szent-Gyorgyi isolated ascorbic acid ( $\text{H}_2\text{A}$ ) from the adrenal gland of a cow and named it vitamin C. An insufficient supply of  $\text{H}_2\text{A}$  in the human body causes symptoms of scurvy [1], but excessive  $\text{H}_2\text{A}$  results in stomach convulsions [2].  $\text{H}_2\text{A}$  promotes healthy cell development, normal tissue growth, and the healing of injuries and burns [3]. It helps in the synthesis of collagen, an important component of ligaments, blood vessels, cartilage, bones, and tendons [4]. Physiologists are devoting increasing attention to the quantitative measurement of  $\text{H}_2\text{A}$ .

The direct measurement of the amount of ascorbic acid in the human body is difficult because ascorbic acid is water soluble, acts as an antioxidant, and is not stored in the body. Various researchers have developed  $\text{H}_2\text{A}$  sensors with specific functions and advantages. Sensors based on ion-sensitive field-effect transistors (ISFETs) are highly stable and respond quickly, but ISFET lithography is expensive [5]. Optical  $\text{H}_2\text{A}$  sensors can detect  $\text{H}_2\text{A}$  in a reaction mixture, but various environmental factors, e.g., chemical disturbances, temperature, and optical conditions, can limit the effectiveness of such sensors [6]. Conductometric sensors can be operated with ease but often exhibit unsatisfactory sensitivity, selectivity, and accuracy levels [7]. Potentiometric sensors can be effective even if they use miniature working areas; however,

potentiometric sensors are often limited by slow response times and ionic noise from the solution [8].

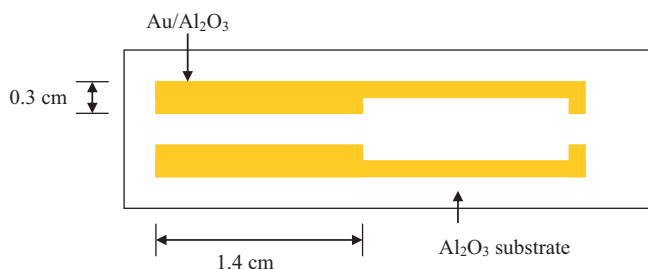
Amperometric sensors can be made to overcome the disadvantages of other sensors. An amperometric sensor is usually designed as a laminate structure with a metal film on top of an active layer, which is, in turn, on top of a substrate. The metal film is proportionally sensitive to specific chemicals. Amperometric sensors respond to  $\text{H}_2\text{A}$  quickly and can detect a wide range of  $\text{H}_2\text{A}$  concentrations [9–13]. Many amperometric sensors contain modifier metals in their metal films to enhance the electrode response. In this study, we used platinum as the  $\text{H}_2\text{A}$ -sensitive metal matrix [14–16] and nickel as the modifier metal because nickel is chemically similar to platinum. The Pt-lean (Pt content less than 50%) and Pt-rich (Pt content greater than 50%) alloys were employed to sense  $\text{H}_2\text{A}$  simultaneously. However, the Pt-lean alloys are less sensitive than Pt-rich alloys for  $\text{H}_2\text{A}$  oxidation, which is not presented in this paper. We further confirmed the modifying theorem in which the rich component, Pt, is the sensing metal and the lean component, Ni, serves as a modifier to enhance the sensitivity by intensifying the electrode's specific area. After a series of electrochemical tests, we found that the Ni–Pt alloys were more sensitive than either Ni or Pt in isolation.

## 2. Experimental

### 2.1. Fabrication of the Ni–Pt electrode

An alumina board was cut into slices, each of which measured 3.5 cm × 1.5 cm × 0.1 cm. These slices were cleaned ultrasonically

\* Corresponding author. Tel.: +886 4 24517250x3689; fax: +886 4 24510890.  
E-mail address: [ycweng@fcu.edu.tw](mailto:ycweng@fcu.edu.tw) (Y.-C. Weng).



**Scheme 1.** The screen printing pattern for the conductive Au paste.

in an acetone bath for 20 min to remove the organic coating. The cleaned slices were then rinsed with deionized (DI) water and dried in an oven at 100 °C for 20 min. A “doctor blade” screen-printing process [14] was used to deposit conductive gold paste (Heraeus C-5754B, 87.5%) onto each aluminum substrate to form the pattern shown in Scheme 1. Each as-printed substrate was maintained at 150 °C for 40 min to evaporate the solvent in the paste and was then heated in a furnace (CHEMIST DF20) at 850 °C for 40 min to sinter the gold layer. Each as-sintered substrate was soaked in an acetone bath for 30 min and then cleaned in DI water for 30 min.

The electrode layers were prepared by electrodeposition. A reference electrode made of Ag/AgCl (KCl sat'd) was configured to maintain a standard applied potential. To prevent inhomogeneous deposition, a stirring plate was used to agitate all the deposition solutions. For the pure Pt layer, a solution of 0.01 M  $\text{H}_2\text{PtCl}_6 \cdot 6\text{H}_2\text{O}$  (dihydrogen hexachloroplatinate (IV) hexahydrate 99.9%, UR) was used at an applied potential of  $-100\text{ mV}$  in a potentiostat (CHI 824B). For the pure Ni layer, a solution of 1 M  $\text{NiCl}_2 \cdot 6\text{H}_2\text{O}$  (nickel chloride hexahydrate, SHOWA, 96%) was used at an applied potential  $-800\text{ mV}$ . The deposition rate between Ni and Pt strongly depends on the applied potential. We therefore adjusted the alloy composition by increasing the deposition rate of Ni and reducing the deposition rate of Pt. The distinct applied potentials were applied to differentiate the composition of the Ni–Pt alloys. A solution of 0.01 M  $\text{H}_2\text{PtCl}_6 \cdot 6\text{H}_2\text{O}$  was blended with a solution of 1 M  $\text{NiCl}_2 \cdot 6\text{H}_2\text{O}$ , and potentials of  $-200\text{ mV}$ ,  $-400\text{ mV}$ , and  $-600\text{ mV}$  were applied. All depositions were performed for 10 min.

## 2.2. Instruments for the investigation of the electrode

The morphology of each electrode was investigated with a scanning electron microscope (Hitachi 3000-H). Electrode compositions were measured with an energy-dispersive spectrum analyzer (Noran Voyager 2.0). The crystallization of the Ni–Pt alloys was measured with a thin-film X-ray diffractometer (XRD) (Bruker D8-SSS).

## 2.3. Preparation of the test solution

Ascorbic acid ( $\text{C}_6\text{H}_8\text{O}_6$ , L-(+)-ascorbic acid 99%, Acros) was diluted to serve as a stock solution for the subsequent blending. The alkaline test solution was a blank solvent that contained 0.1 M KOH (85%, Showa). The interference reagents for the  $\text{H}_2\text{A}$  test were anhydrous oxalic acid (99%,  $\text{H}_2\text{C}_2\text{O}_4$ , Showa), sucrose (>99.9%,  $\text{C}_{12}\text{H}_{22}\text{O}_{11}$ , Showa), sodium benzoate (99%,  $\text{C}_6\text{H}_5\text{COONa}$ , Showa), L-(+)-tartaric acid (99%,  $\text{C}_4\text{H}_6\text{O}_6$ , Showa), D-(–)-fructose (99%,  $\text{C}_6\text{H}_{12}\text{O}_6$ , Acros), and anhydrous citric acid (99%,  $\text{C}_3\text{H}_4(\text{OH})(\text{COOH})_3$ , Showa).

## 3. Results and discussion

### 3.1. Microstructure investigation of the Ni–Pt electrode

#### 3.1.1. Morphology investigation

The portion of the Ni–Pt electrode with a Ni matrix contained agglomerated spinodal crystals whereas the portion with a Pt matrix was characterized by coarse grains. The local morphology of the Ni–Pt electrode varied according to the local matrix. Fig. 1(a) shows an erinaceous surface that was observed on a Ni crystal. Ni film was particularly notable on the embedded needles. The three images of Fig. 1(b)–(d) show how Pt caused the spinodal surfaces to mix with the particle phases. These images indicate that Pt atoms affected crystallization as they blended into the Ni crystal lattices. Fig. 1(e) shows a surface for which all spinodal crystals were replaced with coarse particles. The high sensitivity of the surface was determined by two conditions: a high specific area, *i.e.*, high surface area per unit weight of crystal, and a sensitive preferred crystal orientation on the electrode [17]. Fig. 1(a) shows a spinodal surface with a large specific area; Fig. 1(e) shows a coarse surface littered with agglomerate particles. With regard to the preferred crystal orientation, we discuss in Section 3.1.2 how crystallization can be identified by diffraction patterns.

#### 3.1.2. Composition-induced phase transformation in the Ni–Pt alloys

An alloy that incorporates Ni into a Pt matrix is expected to exhibit a porous morphology. Fig. 2 shows a series of X-ray diffraction patterns for the Ni–Pt alloys. The intensities of the Au(1 1 1) peaks in both pure Ni and pure Pt are smaller than those in  $\text{Pt}_{61}\text{Ni}_{39}$ ,  $\text{Pt}_{70}\text{Ni}_{30}$ , and  $\text{Pt}_{82}\text{Ni}_{18}$  because the Au(1 1 1) signal originates from the sub-layer. A lower Au(1 1 1) intensity reflects a smaller exposed Au sub-layer area. A small exposed sub-layer area results in a large exposed deposited layer. We concluded that the porous morphologies of the alloyed compositions  $\text{Pt}_{61}\text{Ni}_{39}$ ,  $\text{Pt}_{70}\text{Ni}_{30}$ , and  $\text{Pt}_{82}\text{Ni}_{18}$  tended to reflect signals from the substrates.

The intermetallic compounds (IMCs) of the Ni–Pt alloys exerted critical effects on the microstructural variations of the electrodes. Fig. 2 shows that a Pt(1 1 1) peak was present for all compositions except pure Ni. Pure Ni does not show this peak, but materials with some Pt show a peak proportional to the amount of Pt. This result indicates that the Pt component enhanced the Pt(1 1 1) preferred orientation. Only pure Ni displayed the Ni(2 0 0) peak. This result suggests that the Ni lattice was reconstructed as soon as Pt atoms infiltrated the Ni matrix. We further confirmed the result that only two IMCs,  $\text{Ni}_3\text{Pt}$  and  $\text{NiPt}_3$ , contributed to the intermediate compositions  $\text{Pt}_{61}\text{Ni}_{39}$ ,  $\text{Pt}_{70}\text{Ni}_{30}$ , and  $\text{Pt}_{82}\text{Ni}_{18}$ ; details are provided in Appendix A.

### 3.2. The electrochemical reaction on the electrode

#### 3.2.1. Cyclic voltammetry

The results of the cyclic voltammetry (CV) tests were complicated by faradic and non-faradic currents that contributed to the peak shifts in this study. The following paragraphs describe the results of CV tests on the Pt, Ni–Pt and Ni electrodes with both blank and  $\text{H}_2\text{A}$ -containing solutions.

The Pt electrode was found to be sensitive to ascorbic acid. The CV measurement of Pt subjected to  $\text{H}_2\text{A}$  is shown in Fig. 3. In the blank solution, the response current in the forward scan increased appreciably at  $-0.68\text{ V}$  and  $-0.62\text{ V}$ , as shown by the dashed line. The first peak was related to the desorption process for the weakly bound hydrogen ions on the electrode; the second peak showed the desorption process for hydrogen atoms strongly bound to platinum [18]. Pitara and co-workers investigated the preferred orientations of the adatom peaks; they found

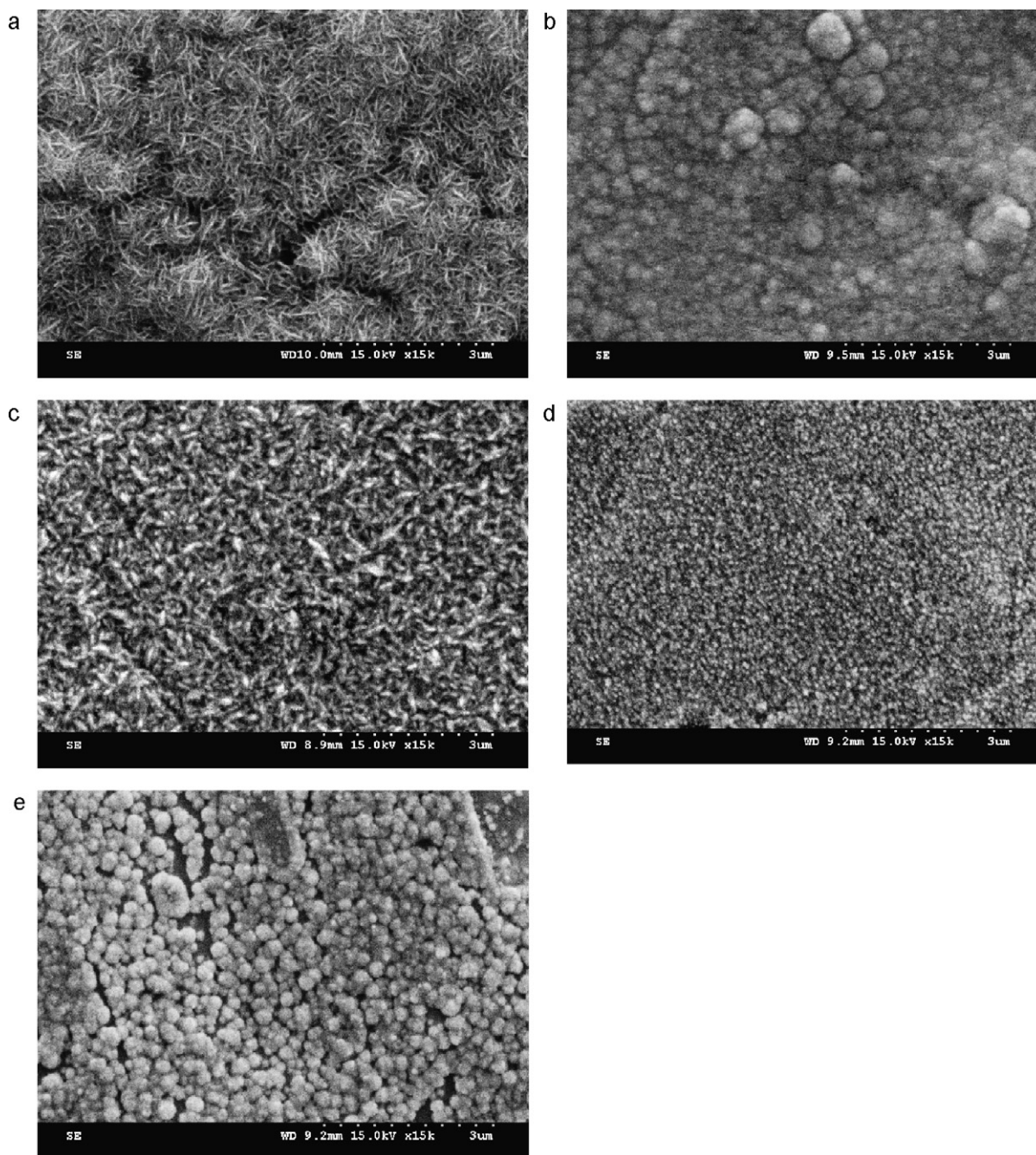


**Fig. 1.** SEM images of the Pt–Ni alloy electrodes. (a) Ni; (b) Pt<sub>61</sub>Ni<sub>39</sub>; (c) Pt<sub>70</sub>Ni<sub>30</sub>; (d) Pt<sub>82</sub>Ni<sub>18</sub>; (e) Pt on Au/Al<sub>2</sub>O<sub>3</sub> substrates.

that the first peak usually occurs on the Pt(1 1 0) orientation and that the second peak preferred the Pt(1 0 0) orientation [19]. Both of these responses occurred on the polycrystalline Pt electrode. No obvious reduction peak was observed in the reverse scan to couple with the adsorption process, which suggests that the electrode might have been poisoned and that the reduction current might have been inhibited. Gasteiger et al. researched the oxidation of CO/H<sub>2</sub> mixtures on Pt–Ru alloys and found that even trace amounts of CO negatively shifted the potential [20]. Igarashi et al. studied electro-oxidation on Pt catalysts and concluded that the type of CO bonding on Pt sites depended on the CO coverage [21]. These results imply that the CO exclusively occupied the active sites of the electrode and repelled the hydrogen ions [22]. The reduction peak appeared only when the applied voltage was extended to negative potentials beyond the measured range of this study.

When the forward scan voltage was increased, a plateau appeared at  $-0.1$  V because of Pt oxidation current on the electrode. In the reverse scan, a conspicuous peak appeared at  $-0.28$  V because of PtOx reduction. The voltammogram for the H<sub>2</sub>A-containing solution showed a distinct response, as shown by the solid line in Fig. 3. Two broad peaks for the adsorption/desorption processes still appeared at  $-0.65$  V and  $-0.45$  V, but they shifted forward. Two waveform peaks were observed at 0.14 V and 0.35 V. The first peak, at 0.14 V, represented a series of oxidation processes with the product 2,3-diketogulonic acid (DKG); the second peak showed the oxidation of the DKG. Either the first or the second peak showed a two-electron process, which means the oxidation was not a single-electron reaction. These two peaks showed broad waveforms and high current intensities. Oxidation of Pt electrode itself also occurred simultaneously in this potential region. Thus,

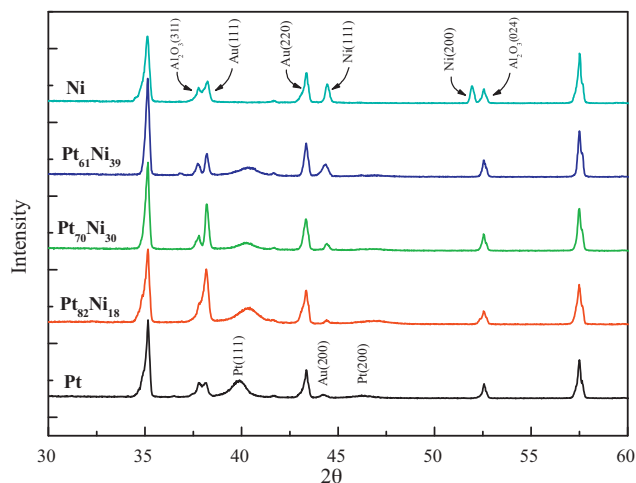
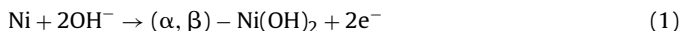


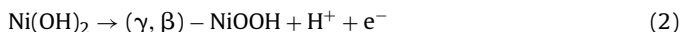
Fig. 2. X-ray diffraction patterns of the Pt<sub>x</sub>Ni<sub>y</sub> electrodes.

a small, single reduction peak appeared at 0.0 V in the reverse scan, which represented the reduction of PtOx on the electrode [23].

Fig. 4 shows the CV curves for a Ni electrode in both a blank and an H<sub>2</sub>A-containing solution. In the blank solution, the response current increased appreciably at -0.03 V, as indicated by the dashed line. This increase was due to the electrochemical reaction between the Ni and the hydroxyl ion; α-Ni(OH)<sub>2</sub> and β-Ni(OH)<sub>2</sub> remained on the electrode [24]. The reaction can be expressed as follows:



When the applied voltage was increased to 0.46 V, β-type and γ-type Ni peroxide formed immediately. This phase transformation was accompanied by an electron transfer, which occurred on the electrode as expressed in the following formula [14]:



Furthermore, considerable amounts of γ-type Ni oxide formed by oxidation of γ-NiOOH. This process can be described by the following expression [25]:



The formation of NiOOH and NiO<sub>2</sub> contributed to the peak at 0.46 V. The reduction peak appeared at 0.36 V in the reverse scan.

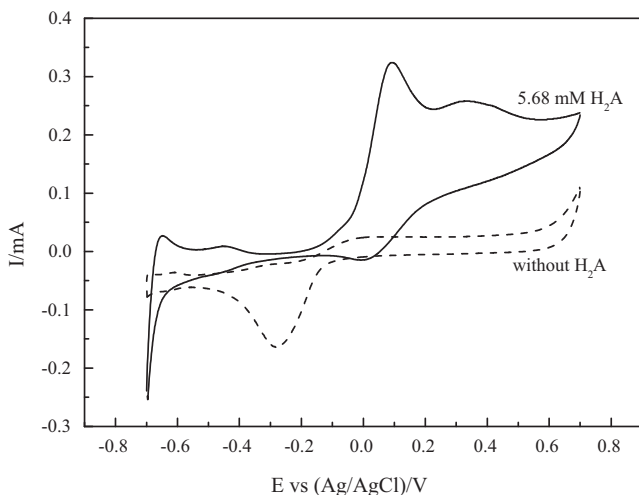


Fig. 3. Cyclic voltammetric behaviors of a Pt electrode (---) without H<sub>2</sub>A and (—) with 5.68 mM H<sub>2</sub>A in 0.1 M KOH solution.

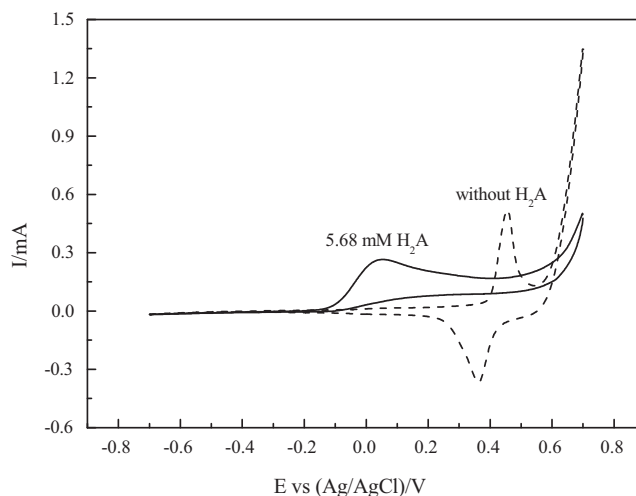
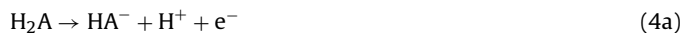


Fig. 4. Cyclic voltammetric behaviors of a Ni electrode (---) without H<sub>2</sub>A and (—) with 5.68 mM H<sub>2</sub>A in 0.1 M KOH solution.

In contrast to the blank solution reaction, the reduction peak at 0.36 V disappeared from Fig. 4 when the test solution contained H<sub>2</sub>A. This process is shown by the solid line in Fig. 4. When the H<sub>2</sub>A molecule approached the Ni electrode, it adsorbed on the surface of Ni. The H<sub>2</sub>A molecule was then electro-activated to hydrate and to release hydrogen ions; therefore, the zeta potential was changed and the local pH value near the electrode was reduced. The decrease in pH inhibited the Ni(OH)<sub>2</sub> oxidation as described in Eq. (2), but it still allowed a series of oxidations to contribute a peak at 0.04 V as described by:



where HA<sup>-</sup> and A<sup>2-</sup> represent C<sub>6</sub>H<sub>7</sub>O<sub>6</sub><sup>-</sup> and C<sub>6</sub>H<sub>6</sub>O<sub>6</sub><sup>2-</sup>, respectively.

Fig. 5 shows the CV tests for the Pt<sub>82</sub>Ni<sub>18</sub> electrode in both blank and H<sub>2</sub>A-containing solutions. The Ni–Pt alloys showed considerable voltage shifts in the CV test with the H<sub>2</sub>A-containing solution. When the Pt<sub>82</sub>Ni<sub>18</sub> electrode was scanned at positive potentials above -0.51 V in the blank solution, the formation of Pt<sub>x</sub>Ni<sub>y</sub>O<sub>z</sub> occurred. The oxidation of Pt<sub>w</sub>Ni<sub>1-w</sub>(OH)<sub>2</sub> took place at potentials greater than 0.45 V whereas the reduction of Pt<sub>w</sub>Ni<sub>1-w</sub>(OOH)

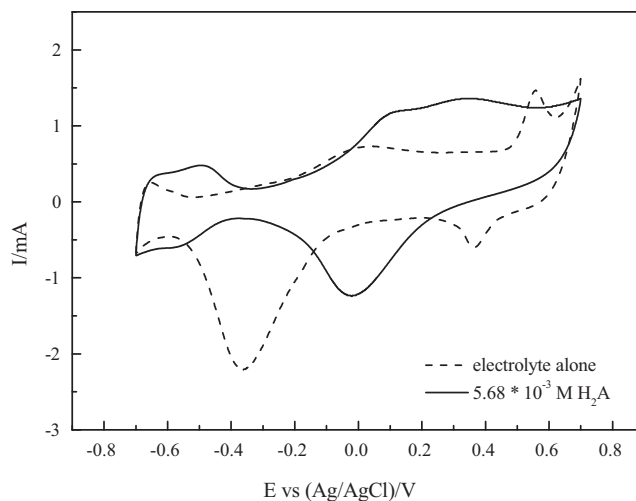
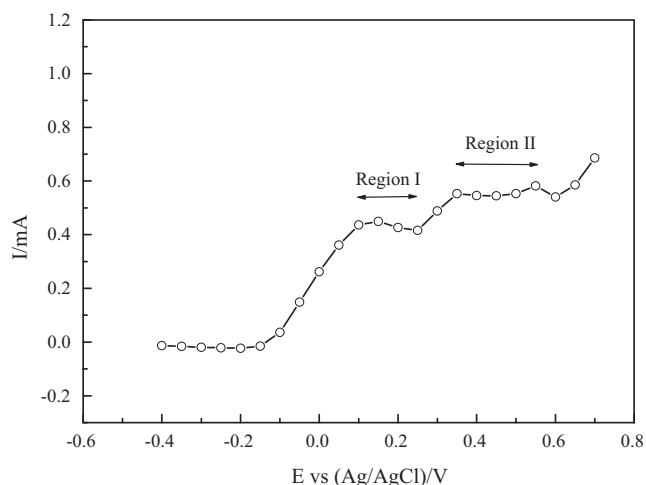


Fig. 5. Cyclic voltammetric behavior of a Pt<sub>82</sub>Ni<sub>18</sub> electrode (---) without H<sub>2</sub>A and (—) with 5.68 mM H<sub>2</sub>A in 0.1 M KOH solution.



**Fig. 6.** The polarization curve of a Pt<sub>82</sub>Ni<sub>18</sub> electrode with 5.68 mM H<sub>2</sub>A in 0.1 M KOH solution.

commenced at 0.5 V in the reverse scan. A large Pt<sub>x</sub>Ni<sub>y</sub>O<sub>z</sub> reduction peak appeared at  $-0.36$  V. In the presence of H<sub>2</sub>A, the peaks that correspond to hydrogen adsorption and desorption appear at potentials between  $-0.7$  and  $-0.4$  V. The two peaks at 0.11 V and 0.32 V in the forward scan were related to the initial oxidation of the H<sub>2</sub>A and to its further oxidation, respectively. The oxidation of the Pt<sub>82</sub>Ni<sub>18</sub> electrode also occurred simultaneously in the forward scan. Therefore, a distinct reduction peak of Pt<sub>x</sub>Ni<sub>y</sub>O<sub>z</sub> appeared at  $-0.02$  V in the reverse scan. We concluded that the Ni–Pt alloy permitted the H<sub>2</sub>A electrochemical reaction. The results suggested that Pt alloyed with Ni possesses an outstanding sensitivity for H<sub>2</sub>A, which benefits from particular microstructural variations of the Ni–Pt alloys, as discussed in Sections 3.1.1 and 3.1.2.

### 3.2.2. Polarization curves for applied potentials

The applied potentials were determined using polarization curves. Fig. 6 shows the polarization curve by which both the polarizing current and the applied potential were determined. The response current for an H<sub>2</sub>A-containing solution exhibited two stepwise variations that are shown with hollow symbols in Fig. 6. The first step, from  $-0.1$  V to 0.25 V, contained a ramp and a flat region; this behavior indicated kinetics-controlled and diffusion-controlled processes. For the kinetics-controlled process, the current was increased because it related to the oxidation rate of H<sub>2</sub>A. The characteristics of the kinetics-controlled process produced a rush current in a high concentration of H<sub>2</sub>A. This rush current tended to prolong the disturbance time and prevent a stable response; therefore, the applied potential had to be excluded for the kinetics-controlled process. In the flat region, labeled region I, the current reached a constant value that was independent of the reaction rate because of a diffusion-controlled process. From 0.25 V to 0.50 V, the secondary oxidation of H<sub>2</sub>A produced another flat region, labeled region II. A higher voltage applied in region II induced unnecessary responses from interferences, which disturbed the measurement process. Thus, the applied potential data were taken from range I, where the mathematical average potential was 0.2 V.

### 3.2.3. Chronoamperometric tests

H<sub>2</sub>A concentration calibration curves were constructed for all Ni–Pt electrodes. Fig. 7(a) shows the response current for the Pt electrode in 0.1 M KOH solution with a fixed applied potential of 0.2 V. The response current increased stepwise for each 0.57 mM increase in H<sub>2</sub>A. With the increase in the H<sub>2</sub>A concentration, the noise increased because the large response current attracted stray

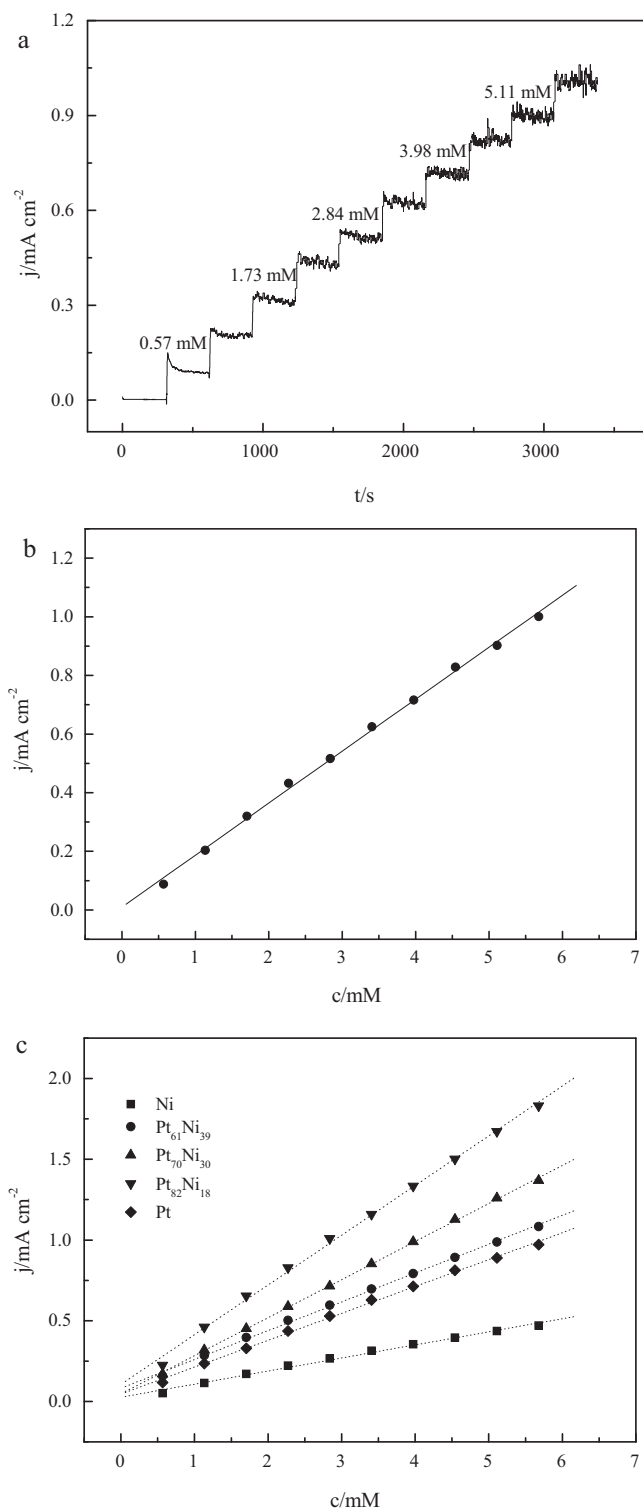


**Fig. 7.** (a) Amperometric response of a Pt electrode in 0.1 M KOH solution at an applied potential of 0.2 V with a successive additions of H<sub>2</sub>A in the concentration range of 0.57–5.68 mM. (b) The calibration curves fitted with a linear regression. (c) The calibration curves of the Pt<sub>x</sub>Ni<sub>y</sub> alloy electrodes in 0.1 M KOH solution at an applied potential of 0.2 V with successive additions of H<sub>2</sub>A in the concentration range of 0.57–5.68 mM. Symbols: (■) Ni/Au/Al<sub>2</sub>O<sub>3</sub>; (●) Pt<sub>61</sub>Ni<sub>39</sub>; (▲) Pt<sub>70</sub>Ni<sub>30</sub>; (▼) Pt<sub>82</sub>Ni<sub>18</sub>; (◆) Pt/Au/Al<sub>2</sub>O<sub>3</sub>.

**Table 1**  
Various types of amperometric sensors.

| Electrode   | Electrolyte  | Linear range (M)                              | Sensitivity ( $\mu\text{A cm}^{-2} \text{mM}^{-1}$ ) | Detection limit (mM)  | Ref  |
|---|--|---|--|-----------------------|------|
| GCE modified with ferricyanide-doped Tosflex  | Phosphate buffer (pH = 5)                              | $1 \times 10^{-6}$ – $5 \times 10^{-5}$       | 120 <sup>a</sup>                                     | –                     | [26] |
| GCE modified with vanadium oxide<br>(VO(OC <sub>3</sub> H <sub>7</sub> ) <sub>3</sub> ) polypropylene carbonate                     | Britton–Robinson (pH = 8.06)                           | $4 \times 10^{-8}$ – $1 \times 10^{-4}$       | 406  | –                     | [27] |
| SPCE modified with drop-casting of<br>dodecylbenzene sulfonic acid (DBSA)-doped<br>polyaniline nanoparticles                        | Phosphate buffer (pH = 6.8)                            | $5 \times 10^{-4}$ – $8 \times 10^{-3}$       | 10.75  | $8.3 \times 10^{-3}$  | [28] |
| AGCE and AuE modified with ascorbate<br>oxidase (ASOD) micelle membrane   | Phosphate buffer (pH = 5.5)                            | $5 \times 10^{-6}$ – $4 \times 10^{-4}$       | 10.85 (AGCE)   | –                     | [10] |
| GCE modified with electrodeposited films<br>derived from dihydroxy-benzaldehyde   | Phosphate buffer (pH = 7)                              | $2 \times 10^{-3}$ – $3 \times 10^{-3}$       | 0.44 (2,5-DHB)                                       | 0.16 (2,5-DHB)        | [12] |
| GCE modified with<br>octacyanomolybdate-doped<br>poly(4-vinylpyridine)  | 0.1 M H <sub>2</sub> SO <sub>4</sub>                   | $1 \times 10^{-5}$ – $9.8 \times 10^{-4}$     | 687  | $5.5 \times 10^{-3}$  | [29] |
| Screen-printing ruthenium dioxide electrode   | Phosphate buffer (pH = 7.4)                            | $0$ – $4 \times 10^{-3}$                      | 2.67   | 1.1                   | [30] |
| SPCE modified with MWNTs/PVI-Os multilayer<br>films   | Phosphate buffer (pH = 7)                              | $5 \times 10^{-7}$ – $7 \times 10^{-5}$       | 12.5 <sup>a</sup>                                    | $3 \times 10^{-4}$    | [31] |
| Graphite electrode modified with polypyrrole<br>nanowire  | 0.1 M phosphates                                       | $5 \times 10^{-4}$ – $2 \times 10^{-2}$       | 46.51  | $4.65 \times 10^{-2}$ | [32] |
| GCE modified with poly(glutamic acid)   | Phosphate buffer (pH = 5)                              | $1.2 \times 10^{-7}$ – $2.5 \times 10^{-4}$   | 460 <sup>a</sup>                                     | $4 \times 10^{-5}$    | [33] |
| Boron-doped diamond electrode modified<br>with ferrocyanide-trapped PDMA film   | Phosphate buffer (pH = 7)                              | $1 \times 10^{-6}$ – $3 \times 10^{-5}$       | 233  | –                     | [34] |
| Thermally pre-treated iron electrodes<br>modified with polypyrrole and ferrocyanide<br>ions Fe(CN) <sub>6</sub> <sup>3-</sup> (FCN) | Phosphate buffer (pH = 7)                              | $5 \times 10^{-4}$ – $9 \times 10^{-3}$       | 120  | 0.15                  | [35] |
| Carbon ceramic electrodes modified with<br>terbium hexacyanoferrate   | 0.5 M KCl (pH = 7)                                     | $5 \times 10^{-7}$ – $1 \times 10^{-4}$       | 138.8 <sup>a</sup>                                   | $2 \times 10^{-4}$    | [36] |
| Hexacyanoferrate (II/III) and poly-D-lysine was<br>immobilized on a gold electrode modified<br>with cysteamine                      | TRIS buffer (pH = 7)                                   | $1 \times 10^{-6}$ – $9.1 \times 10^{-4}$     | 62.9   | $2.2 \times 10^{-3}$  | [37] |
| Carbon paste electrode modified with<br>(silica/aniline, Si–An)/(Congo red, CR)   | 0.5 M KCl (pH = 7)                                     | $7.9 \times 10^{-4}$ – $6.7 \times 10^{-3}$   | 4.53   | –                     | [38] |
| GCE modified with Ni(Me <sub>2</sub> (CH <sub>3</sub> CO) <sub>2</sub><br>tetraenoN <sub>4</sub> ) complex                          | Phosphate buffer (pH = 6.6)                            | $0$ – $6.2 \times 10^{-3}$                    | 23.3   | $3.1 \times 10^{-4}$  | [37] |
| Nickel electrode modified with polyaniline<br>(PANI)  | 0.1 M H <sub>2</sub> SO <sub>4</sub>                   | $5 \times 10^{-3}$ – $3.5 \times 10^{-2}$     | 190  | –                     | [39] |
| The electrochemical copolymerization of<br>3,4-dihydroxybenzoic acid and aniline at<br>microdisk gold electrode                     | Phosphate buffer (pH = 6.6)                            | $1 \times 10^{-4}$ – $1 \times 10^{-2}$       | 240 <sup>a</sup>                                     | $5 \times 10^{-2}$    | [13] |
| Carbon paste electrode modified with<br>( $\beta$ -cyclodextrin)–ferrocene inclusion<br>complex                                     | NH <sub>3</sub> –NH <sub>4</sub> Cl buffer (pH = 10.0) | $5 \times 10^{-7}$ – $1 \times 10^{-5}$       | 65.5 <sup>a</sup>                                    | $5 \times 10^{-4}$    | [40] |
| Pt foil   | 0.1 M KOH  | $5.68 \times 10^{-4}$ – $5.68 \times 10^{-3}$ | 178  | –                     | [43] |
| Ni foil   | 0.1 M KOH  | $5.68 \times 10^{-4}$ – $5.68 \times 10^{-3}$ | 169  | –                     | [43] |
| Ni–Pt alloys (this study)   | 0.1 M KOH  | $5.68 \times 10^{-4}$ – $5.68 \times 10^{-3}$ | 333  | –                     | –    |

<sup>a</sup> Geometric area is unknown (unit =  $\mu\text{A cm}^{-2}$ ).

ions over the active site of the electrode. This dependence was replotted and fitted with a linear relationship to obtain the electrode's sensitivity,  $177 \mu\text{A cm}^{-2} \text{mM}^{-1}$ , as shown in Fig. 7(b). Fig. 7(c) shows calibration curves for the Ni–Pt electrodes. The sensitivities follow the inequality  $\text{Pt}_{82}\text{Ni}_{18} > \text{Pt}_{70}\text{Ni}_{30} > \text{Pt}_{61}\text{Ni}_{39} > \text{Pt} > \text{Ni}$ . The mid-composition Ni–Pt alloys –  $\text{Pt}_{82}\text{Ni}_{18}$ ,  $\text{Pt}_{70}\text{Ni}_{30}$ , and  $\text{Pt}_{61}\text{Ni}_{39}$  – exhibited higher sensitivities than the pure metals, Ni and Pt. The sensitivity of pure Ni was so low that it was almost negligible. We propose that, in the bimetallic sensors presented here, Pt was the main component that sensed H<sub>2</sub>A, and Ni was a relatively inert component. The Ni did not exhibit high sensitivity, but enhanced the sensor by varying its microstructure, as discussed in Sections 3.1.1 and 3.1.2. The alloying of the Ni component in the Pt matrix induced a preferred sensitive orientation with a spinodal morphology that enlarged the sensor's specific area and provided more sensing sites. Thus, the sensitivity levels of the mid-composition Ni–Pt alloys –  $\text{Pt}_{82}\text{Ni}_{18}$ ,  $\text{Pt}_{70}\text{Ni}_{30}$ , and  $\text{Pt}_{61}\text{Ni}_{39}$  – were notably high.

The Ni–Pt ascorbic acid sensor performed better than other amperometric sensors. Table 1 lists the sensitivity levels of various ascorbic acid sensors. Excluding sensors with carbon-based electrodes, the Ni–Pt electrode (described in this study) showed a very high sensitivity of  $333 \mu\text{A cm}^{-2} \text{mM}^{-1}$ .

### 3.3. Reliability of the Ni–Pt sensor

#### 3.3.1. The effect of pH value on the sensitivity

The pH values of the analyzed solutions dominated the electrochemical kinetics; either an alkaline solution or an acidic solution could work as an analyzed solution. In acidic solutions, the hydrogen ions of H<sub>2</sub>A were difficult to decompose because the high concentration of hydrogen ions in the solutions created a co-ion effect. The H<sub>2</sub>A might have directly oxidized with the release of two electrons, as described in Eqs. (4a) and (4b); these intermediates might have further hydrolyzed to become hydrated dehydroascorbic acid in an acidic solution. Inversely, the hydrogen ion is apt to dissociate in an alkaline solution at pH = 10–11. Ruiz and co-workers researched the oxidation mechanism in alkaline solution and found a reaction order of “–2.” In our study, as the alkalinity was increased to pH 12–13, the H<sub>2</sub>A dissociated two hydrogen ions to produce DKG. The reaction order was “–1” because the hydroxide ion in the alkaline solution tended to neutralize with the decomposed hydrogen ions. The reactions described in Eqs. (4a) and (4b) went forward according to LeChatelier's principle. The alkaline solution was capable of producing high sensitivity and was therefore adopted in this study.

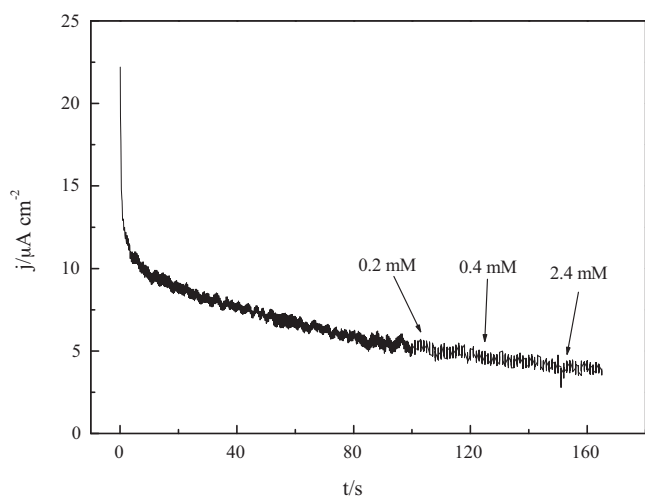


**Fig. 8.** Response current vs. elapsed time for different blending concentrations of uric acid, 0.2 mM, 0.4 mM, and 2.4 mM, in the 0.1 M KOH solution.

### 3.3.2. Response time

The response time followed a diffusion-controlled process caused by the fast redox reaction on the electrode. The reaction rate was determined by the diffusion of the reactant. For dilute solutions, the gradients of the  $H_2A$  concentration near the electrode were low; therefore, the driving forces were weak, and the  $H_2A$  molecules required more time to reach the electrode. In contrast, solutions with high  $H_2A$  concentration gradients also had strong driving forces and produced faster response times.

### 3.3.3. Stability test

The sensitivity exhibited a stable value with a small deviation. The as-prepared electrode was tested for 67 days; the standard deviation for the sensitivity was 3.3%. We considered the sensor to have good endurance.

### 3.3.4. Selectivity test

Chemical noise significantly affected the sensitivity of the Ni–Pt electrode. We tested general disturbances from medical auxiliary reagents, including uric acid, glucose, fructose, sucrose, tartaric acid, citric acid, oxalic acid, and sodium benzoate. A series of reagent blending processes were performed to test the electrode's selectivity. For example, uric acid is often a disturbance source for ascorbic

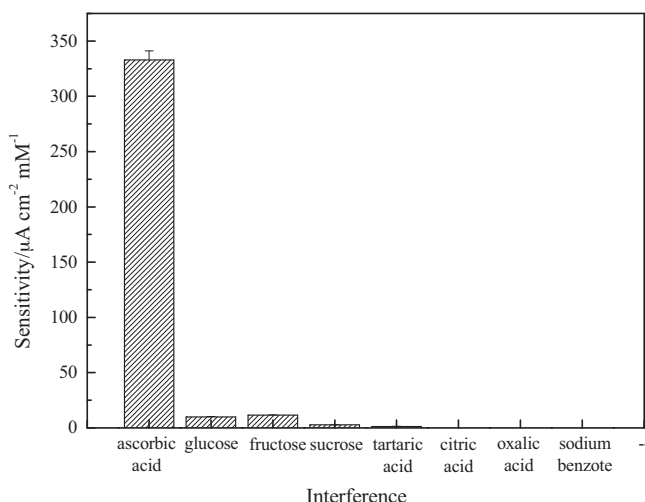


**Fig. 9.** Selectivity of the  $Pt_{82}Ni_{18}$  electrode in 0.1 M KOH solution.

acid measurements. Because its normal concentration in the human body ranges from  $3.6 \text{ mg dl}^{-1}$  to  $8.3 \text{ mg dl}^{-1}$ , a  $6.4 \text{ mg dl}^{-1}$  stock solution of saturated uric acid was blended into the analyzed solution. We observed almost no noise in the response current, as shown in Fig. 8. Fig. 9 shows that very little noise was observed when the other reagents were tested in a similar manner.

## 4. Conclusion

The Ni–Pt electrode showed high sensitivity, endurance, and reliability in this study. We found that the sensing mechanism of the Ni–Pt electrode depended not only on the oxidation of the ascorbic acid in the solution but also on the crystallization of the Ni–Pt itself. In addition, most of the oxidation resulted from charge transfer from Pt rather than from Ni. Although both Pt and Ni were able to sense  $H_2A$ , the Ni–Pt alloy exhibited higher sensitivity than either metal used alone. We attribute the Ni component's enhanced sensitivity to the alloy's erinaceous surface that enlarged the electrode's sensing area.

## Acknowledgements

We gratefully acknowledge support from the National Science Council of the Republic of China (NSC 99-2221-E-035-093) and from Feng Chia University (Grant No. 10G27101).

## Appendix A.

Few articles in the literature have discussed the Ni–Pt phase diagram. Dahmani et al. have published a qualitative series of binary phase diagrams, including a Ni–Pt system [25]. Unfortunately, their Ni–Pt phase diagram is spanned by a complete series of random  $\alpha$ -solid solutions and, because of the long duration of Ni–Pt phase separation, the diagram does not show low temperatures. Theoretical microstructures for Ni–Pt alloys, including Ni,  $Ni_3Pt$ , NiPt,  $NiPt_3$ , and Pt, have been established. Okamoto has reported the Ni–Pt crystal structure data shown in Table A1 [41]. However, no information on the binary Ni–Pt alloy was found in the JCPDS database. We therefore developed theoretical lattices and their diffraction patterns to describe Ni–Pt alloy compositions.

The Ni crystal has been measured: its atomic radius is  $1.62 \text{ \AA}$ , its lattice parameter is  $2.62 \text{ \AA}$ , and its space group is  $Fm\bar{3}m$  [42]. The software package CaRIne was employed to fit the Ni data. The Ni atomic coordination arrangement and its theoretical XRD pattern are shown in Fig. A1. This theoretical pattern was confirmed by the JCPDS data. IMC lattices for  $Ni_3Pt$ , NiPt, and  $NiPt_3$  must be stretched to contain the larger Pt atom, whose atomic radius is  $1.82 \text{ \AA}$  larger (i.e., 10.4% larger) than that of Ni. The IMC lattice was, therefore, fitted with the Pt lattice parameter of  $3.94 \text{ \AA}$ . Figs. A2–A4 show the IMCs' atomic coordination arrangements and their theoretical XRD patterns. The Pt XRD pattern was constructed by applying the data in JCPDS, as shown in Fig. A5. Because the peak at ca.  $40^\circ$  disappeared in the diffraction pattern of NiPt, this alloy was disregarded in this research.

Only part of the intermediate phases between Ni and Pt are presented in this study. Fig. A6 presents a Ni–Pt binary

**Table A1**  
Ni–Pt crystal structure data modeled after the results of Okamoto [41].

| Phase    | Pearson symbol | Space group  | Superlattice structure |
|----------|----------------|--------------|------------------------|
| (Ni, Pt) | cF4            | $Fm\bar{3}m$ | A1                     |
| $Ni_3Pt$ | cP4            | $Pm\bar{3}m$ | L1 <sub>2</sub>        |
| NiPt     | tP4            | $P4/mmm$     | L1 <sub>0</sub>        |
| $NiPt_3$ | cP4            | $Pm\bar{3}m$ | L1 <sub>2</sub>        |

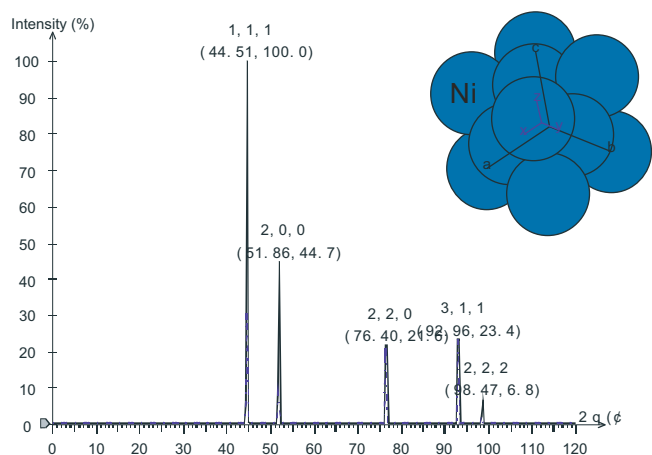


Fig. A1. The theoretical XRD pattern of Ni and its atomic arrangement.

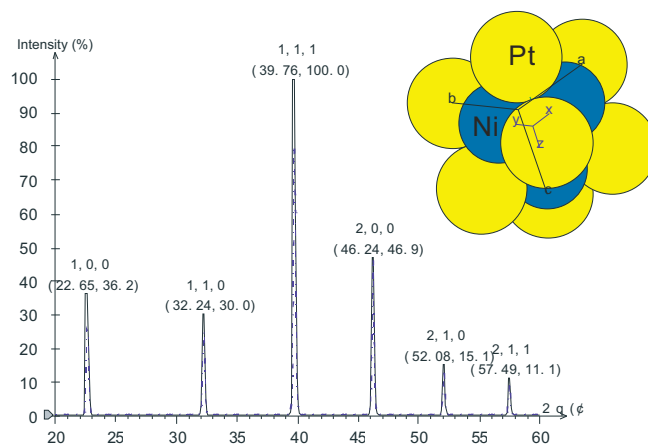


Fig. A4. The theoretical XRD pattern of NiPt<sub>3</sub> and its atomic arrangement.

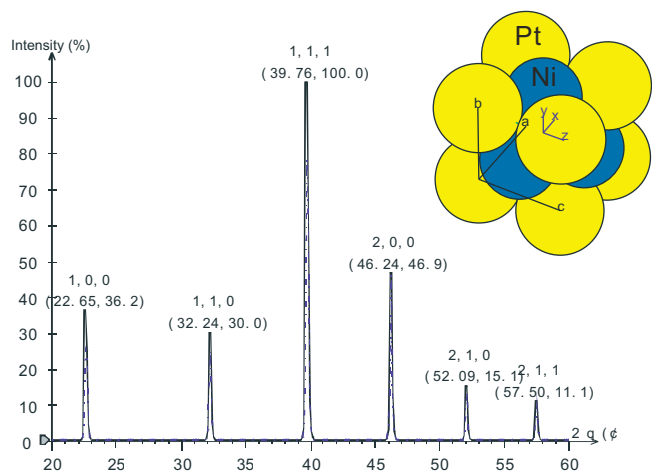


Fig. A2. The theoretical XRD pattern of Ni<sub>3</sub>Pt and its atomic arrangement.

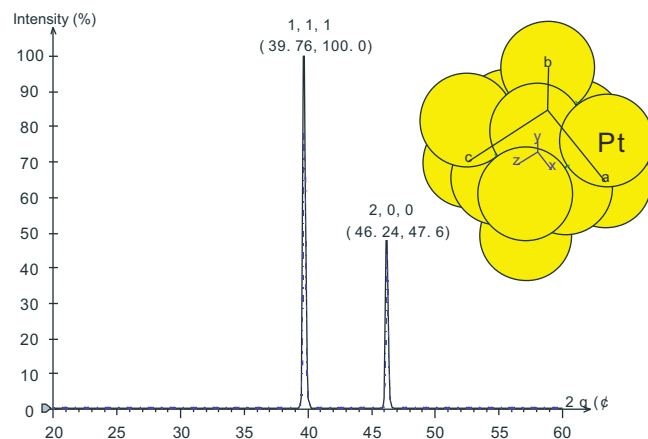


Fig. A5. The theoretical XRD pattern of pure Pt and its atomic arrangement.

phase diagram. Five thermodynamically stable phases exist: Ni, Ni<sub>3</sub>Pt, NiPt, NiPt<sub>3</sub>, and Pt; the theoretical XRD patterns present reconstructed microstructures of these phases. The particular peak at ca. 39.8° in Fig. 2 appeared in most of the diffraction patterns except that of Ni; however, it did not appear in Fig. A3 for the NiPt phase. The NiPt phase was excluded in the alloys containing Pt. The intermediate compositions Pt<sub>61</sub>Ni<sub>39</sub>,

Pt<sub>70</sub>Ni<sub>30</sub>, and Pt<sub>82</sub>Ni<sub>18</sub> exhibited grains that were finer than those in Fig. 1(e) because of the specific coarse-grain morphology of the electrodeposited Pt crystals. The phase of Pt was also excluded in these intermediate compositions. Therefore, the left IMCs, *i.e.*, Ni<sub>3</sub>Pt and NiPt<sub>3</sub>, contributed the intermediate compositions Pt<sub>61</sub>Ni<sub>39</sub>, Pt<sub>70</sub>Ni<sub>30</sub>, and Pt<sub>82</sub>Ni<sub>18</sub>. Ni was regarded as a modifier; it characterizes the preferred crystallizations in this study. However, the lattice parameters of Ni<sub>3</sub>Pt

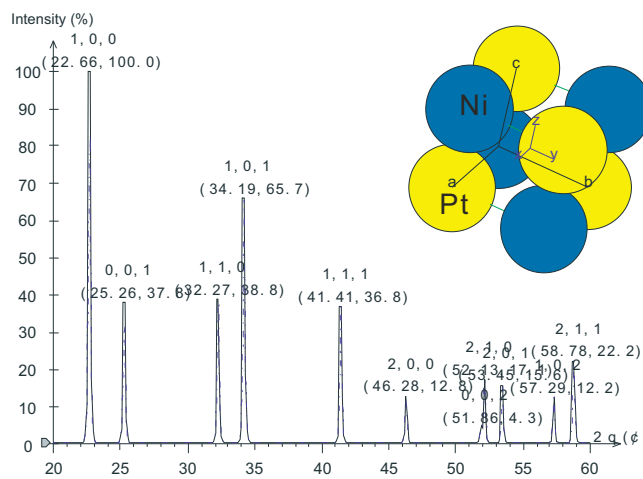


Fig. A3. The theoretical XRD pattern of NiPt and its atomic arrangement.

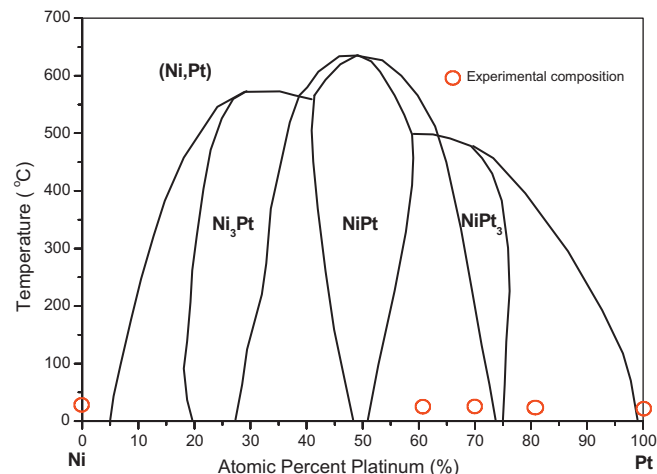


Fig. A6. The Ni–Pt binary phase diagram modeled after the results of Okamoto [41].

and NiPt<sub>3</sub> were still difficult to estimate. The intensities of the secondary strong peaks in Ni<sub>3</sub>Pt and NiPt<sub>3</sub> decreased dramatically in Figs. A2–A4. Only the strongest peaks of Ni<sub>3</sub>Pt and NiPt<sub>3</sub> were discernible in the pattern of the complicated laminate Ni–Pt/Au/Al<sub>2</sub>O<sub>3</sub>. The limited information obtained from the finite strongest peaks could not fit the matrix iteration of the lattice parameters. The exact solution is to be determined in a subsequent analysis.

## References

- [1] S.J. Padayatty, A. Katz, Y. Wang, P. Eck, O. Kwon, J.H. Lee, S. Chen, C. Corpe, A. Dutta, S.K. Dutta, M. Levine, *J. Am. Coll. Nutr.* 22 (2003) 18.
- [2] M. Sönmeza, G. Türk, A. Yüce, *Theriogenology* 63 (2005) 2063.
- [3] B.A. Eipper, R.E. Mains, C.C. Glembotski, *Proc. Natl. Acad. Sci. U.S.A.* 80 (1983) 5144.
- [4] S.J. Klebanoff, D.D. Dziewiatkowski, G.J. Okinaka, *J. Gen. Physiol.* 4 (1958) 303.
- [5] S. Martinoia, G. Massobrio, L. Lorenzelli, *Sens. Actuators B: Chem.* 105 (2005) 14.
- [6] A. Jain, A. Chaurasia, K.K. Verma, *Talanta* 42 (1995) 779.
- [7] S. Ivanow, V. Tsakova, V.M. Mirsky, *Electrochem. Commun.* 8 (2006) 643.
- [8] M.K. Amini, S. Hahrokhian, S. Tangestaninejad, V. Mirkhani, *Anal. Biochem.* 290 (2001) 277.
- [9] M. Arvand, Sh. Sohrabnezhad, M.F. Mousavi, *Anal. Chim. Acta* 491 (2003) 193.
- [10] X. Wang, H. Watanabe, S. Uchiyama, *Talanta* 74 (2008) 1681.
- [11] J.B. Raof, R. Ojani, A. Kiani, *J. Electroanal. Chem.* 515 (2001) 45.
- [12] G. Moreno, F. Pariente, E. Lorenzo, *Anal. Chim. Acta* 420 (2000) 29.
- [13] J.J. Sun, D.M. Zhou, H.Q. Fang, H.Y. Chen, *Talanta* 45 (1998) 851.
- [14] M.I. Manzanares, V. Solis, R.H. de Rossi, *J. Electroanal. Chem.* 430 (1997) 163.
- [15] M.I. Manzanares, V. Solis, R.H. de Rossi, *J. Electroanal. Chem.* 407 (1996) 141.
- [16] A. Serpen, V. Gokmen, *Food Chem.* 104 (2007) 721.
- [17] M.J. Valls, J.M. Feliu, A. Aldaz, M.A. Climent, J. Clavilier, *J. Electroanal. Chem.* 260 (1989) 237.
- [18] J.J. Ruiz, A. Aldaz, M. Dominguez, *Can. J. Chem.* 56 (1978) 1533.
- [19] E.L. Pitara, J. Barbier, *Appl. Catal. A: Gen.* 149 (1997) 49.
- [20] H.A. Gasteiger, N.M. Marković, P.N. Ross Jr., *J. Phys. Chem.* 99 (1995) 16757.
- [21] H. Igarashi, T. Fujino, M. Watanabe, *J. Electroanal. Chem.* 391 (1995) 119.
- [22] L.D. Burke, L.M. Hurley, *Electrochim. Acta* 44 (1999) 3451.
- [23] N.H. Li, S.G. Sun, S.P. Chen, *J. Electroanal. Chem.* 430 (1997) 57.
- [24] X. Xing, I.T. Bae, M. Shao, C.C. Liu, *J. Electroanal. Chem.* 346 (1993) 309.
- [25] C.E. Dahmani, M.C. Cadeville, J.M. Sanchez, J.L. Morán-López, *Phys. Rev. Lett.* 55 (1985) 1208.
- [26] J.M. Zen, D.M. Tsai, A.S. Kumar, V. Dharuman, *Electrochem. Commun.* 2 (2000) 782.
- [27] L. Tian, L. Chen, L. Liu, N. Lu, W. Song, H. Xu, *Sens. Actuators B: Chem.* 113 (2006) 150.
- [28] A. Ambrosio, A. Morrin, M.R. Smyth, A.J. Killard, *Anal. Chim. Acta* 609 (2008) 37.
- [29] R. Thangamuthu, S.M.S. Kumar, K.C. Pillai, *Sens. Actuators B: Chem.* 120 (2007) 745.
- [30] J. Wu, J. Suls, W. Sansen, *Electrochem. Commun.* 2 (2000) 90.
- [31] Y. Sha, L. Qian, Y. Ma, H. Bai, X. Yang, *Talanta* 70 (2006) 556.
- [32] J. Wang, Z. Wang, S. Wang, *Synth. Met.* 156 (2006) 610.
- [33] A.M. Yu, H.Y. Chen, *Anal. Chim. Acta* 344 (1997) 181.
- [34] P.R. Roy, M.S. Saha, T. Okajima, T. Ohsaka, *Electrochim. Acta* 51 (2006) 4447.
- [35] D. Oukil, L. Makhloufi, B. Saidani, *Sens. Actuators B: Chem.* 123 (2007) 1083.
- [36] Q. Sheng, H. Yu, J. Zheng, *J. Electroanal. Chem.* 606 (2007) 39.
- [37] E.S. Ribeiro, L.T. Kubota, *Microchim. Acta* 154 (2006) 303.
- [38] F.A. Pavan, E.S. Ribeiro, Y. Gushikem, *Electroanalysis* 17 (2005) 625.
- [39] R.P. Kalakodimi, M. Nookala, *Anal. Chem.* 74 (2002) 5531.
- [40] Z. Guorong, W. Xiaolei, S. Xingwang, S. Tianling, *Talanta* 51 (2000) 1019.
- [41] H. Okamoto, *J. Phase Equilib. Diffus.* 31 (2010) 322.
- [42] G. Carturan, G. Cocco, S. Enzo, R. Ganzerla, M. Lenarda, *Mater. Lett.* 7 (1988) 47.
- [43] Y.C. Weng, Y.L. Hsiao, *J. Electroanal. Chem.* 651 (2011) 160.